Chapter 7: Hydraulic stimulation of tight geothermal reservoirs

Sri Kalyan Tangirala[1] (tangiralask@gmail.com), *Victor Vilarrasa*[2*]
(victor.vilarrasa@csic.es), *Francesco Parisio*[2,3] (francesco.parisio@protonmail.com)

[1]Department of Applied Geophysics, Indian Institute of Technology (Indian School of Mines) Dhanbad, India.
[2]Global Change Research Group (GCRG), IMEDEA, CSIC-UIB, Esporles, Spain.
[3]Institute of Environmental Assessment and Water Research, Spanish National Research Council (IDAEA-CSIC), Barcelona, Spain.

[*]Corresponding author's email: victor.vilarrasa@csic.es

Abstract

To extend geothermal-energy power generation from hydrothermal systems to places without anomalies in the geothermal gradient, fractures of low-permeability rock– typically at 4-6 km depth to find >150 ºC – should be stimulated to create Enhanced Geothermal Systems (EGS). However, most of the attempts of establishing full-scale EGSs have resulted in high induced seismicity as a result of hydraulic stimulation, leading to project cancellation in some occasions. This has created a big insecurity in further investments into this kind of systems. To achieve the widespread deployment of EGSs alongside existing hydrothermal power plants, we need a thorough understanding of the effect of different hydraulic stimulation strategies on both permeability enhancement and induced seismicity. In this chapter, we compared three stimulation strategies in detail – constant rate, step rate and cyclic injection for a range of dilatancy angles of the stimulated fracture. We find that the extent of fracture reactivation and pressure buildup depends on the injection scheme as well as the dilatancy angle. For a given dilatancy angle, we find that the cyclic injection scheme provides the highest permeability enhancement as well as the highest slip, whereas both of them are observed to be the lowest for the step-rate injection.

7.1 Introduction: Background and Motivation

In Enhanced Geothermal Systems (EGS), hydraulic stimulation aims at increasing the permeability of the crystalline basement to circulate fluids at a rate that is sufficient to produce electricity from geothermal energy (Abe and Horne, 2023). The physical and economic viability of an EGS project strongly depend on the possibility of enhancing the permeability of the reservoir either by propagating new hydraulic fractures or by improving the permeability of existing ones by inducing shear dilation (Parisio and Yoshioka, 2020). Most of the EGSs are typically developed in the crystalline basement (Brown et al., 2012) with high amounts of heat trapped in them. Several field studies involving granitic EGSs have been carried out around the world since the 1970s, e.g., Fenton Hill in the US, Rosemanowes in the U.K., Hijiori in Japan, Cooper Basin in Australia, Soultz-sous-Forêt in France and Basel in Switzerland (reviewed by McClure and Horne, 2014). The typical challenges that occur during EGS stimulation include the inability to sufficiently enhance the permeability of the existing fractures, the difficulties in joining the injection and production wells with a network of permeable fractures (Lepillier et al., 2020), the so-called thermal short-circuiting (Ghassemi, 2012) and induced seismicity (Majer et al., 2007). Induced seismicity proved to be a major roadblock to EGS projects following the events at Basel, Switzerland (Häring et al., 2008) and Pohang, Korea Republic (Ellsworth et al., 2019). In an attempt to maximize permeability enhancement and minimize the magnitude, M, and frequency of the induced earthquakes, a wide range of stimulation protocols have been proposed and employed (McClure and Horne, 2014). Despite the relative abundance, none of the protocols has delivered the expected results: often, the increment of permeability was insufficient (Xie et al., 2015) and/or the magnitude and frequency of the induced earthquakes were above

acceptable levels (Giardini, 2009; Ellsworth et al., 2019). As an example, Traffic Light Systems (TLS) have been devised in an attempt to limit the magnitude and frequency of induced earthquakes during the stimulation stage (Verdon and Bommer, 2021). TLS, however, did not prevent the M3.4 Basel earthquake in December 2004 (Häring et al., 2008) nor the M5.5 Pohang earthquake in November 2017 (Ellsworth et al., 2019).

At Basel, the reactivation of the network of natural fractures occurred during hydro-shearing stimulation with the step-rate injection scheme (Mukuhira et al., 2013). The fractures were reactivated shortly after the beginning of the hydraulic stimulation and the magnitude and frequency of the induced events progressively increased during the six days of injection (Deichmann et al., 2014). The injection was stopped after an event with M>2, but a M3.4 earthquake occurred a few hours after shut-in (Mukuhira et al., 2017). The Basel EGS project was eventually cancelled as a result of the negative impacts caused by induced seismicity (Andrés et al., 2019). It is a common occurrence in induced seismicity that the magnitude of post-injection events is up to 3 orders of magnitude larger than the events occurring during the injection phase in terms of seismic moment. Although the cause of the larger-magnitude post-injection events is likely to be related to poromechanical stress induced by pressure diffusion and shear-slip stress transfer caused by induced microseismic events (Kim and Makhnenko, 2020), we are still far away from an accurate quantification of the driving mechanisms (Segall and Lu, 2015; De Simone et al., 2017).

At Pohang, the cyclic injection protocol was employed during stimulation. A total of five different stimulation stages took place in two separate wells called PX-1 and PX-2. The third and fifth stimulations, both performed at PX-2, induced earthquakes of magnitude 3.1 and 5.5, respectively, in a low-permeable fault located between the two wells (Kim et al., 2018). The M5.5 earthquake, which represents the largest earthquake ever induced by the hydraulic stimulation of an EGS project, also occurred in the post-injection stage and led to project cancellation. The delay between the shut-in and earthquake was of two months at Pohang, much longer than at Basel (Yeo et al., 2021). For the given injected volume, the magnitude was significantly higher than its theoretical maximum as predicted by McGarr's relationship (McGarr, 2014), which is used as the basis for the TLS control in some occasions. The formulations that bound the maximum magnitude to the injected volume have several shortcomings since they do not take into account specific tectonic and geological settings, hydro-geological parameters and injection protocol.

Investigation of the coupled physical processes that govern the response of tight rock to high-pressure injection during hydraulic stimulation is a necessary step to safely conduct EGS operations (Cueto-Felgueroso et al., 2017; Pampillon et al., 2018; Zareidarmiyan et al., 2021). An effective design phase will not only minimize the risks of damage, disruption and potential harm to human life but will also minimize financial risks connected to the project. A thorough characterization accompanied by extensive numerical modelling in the design phase of injection protocols will increase the chances of striking an optimum balance between maximizing productivity (enhancing permeability) and minimizing risks (induced seismicity). This study demonstrates the importance of considering site- and project-specific information in the design of EGS stimulation. We overcome the limitations of the volume-magnitude scaling laws by investigating the impact of the injection protocol on permeability enhancement and induced seismicity. We simulate a series of cases in which the same amount of water is injected into the reservoir but with different injection protocols (scheme and injection rate) and study the response in terms of permeability enhancement and slip induced in the fracture. The constitutive model of the fracture integrates a slip weakening law, and dilation phenomena (Brace et al., 1966). We compare the permeability enhancement and the slip induced along the fracture to assess the effectiveness of the stimulation protocols and find that the cyclic-injection scheme enhances the permeability of a larger area of the fracture compared to the other injection schemes, but at the expense of experiencing a larger slip, which may lead to more induced

seismicity than with the other schemes. The models with step-rate injection induce the least amount of slip in the fracture and induced seismicity as well as the least permeability enhancement.

7.2 Methods

We run bi-dimensional (2D) hydro-mechanical (HM) simulations on a square-shaped granitic reservoir of side length 500 m, where water is injected at the centre of a pre-existing fracture/fault that forms an angle of 70° with the minimum principal stress (Figure 7.1A). The 2D model represents a horizontal plane intersected by a vertical fracture, so gravity is neglected in the simulations. The fracture is modelled as a 10-cm thick continuum medium. We use three different injection schemes: constant rate, step rate and cyclic injection. Additionally, each scheme is composed of three different injection rates: 0.1 kg/s/m, 0.2 kg/s/m and 0.3 kg/s/m applied to the constant and cyclic schemes. There are five cycles in each cyclic scheme, where each cycle comprises an injection interval followed by a no-injection interval of equal duration. The step-rate injection scheme is composed of 5 stages of increasing injection rate, with the different values of flow rates corresponding to the latest stage. To observe the effects of dilatancy on permeability enhancement, we use four values of the dilatancy angle – 0.1^o, 2°, 4° and 10° – for every injection scheme and injection rate. We run a total of 36 simulations – constant-rate scheme with 0.1 kg/s/m rate for 0.1^o dilatancy angle being one example. The amount of water injected into the reservoir is 270 kg/m in all models.

The coupled HM simulations are solved monolithically. For the hydraulic problem, mass conservation of water is given by

$$\frac{\varphi}{K_f}\frac{\partial p}{\partial t} + \nabla.\frac{du}{dt} + \frac{1}{\rho}\nabla.(\rho q) = f_w, \qquad (7.1)$$

where φ is porosity, $\frac{1}{K_f}$ is water compressibility, p is pressure, u is the solid displacement vector, t is time, ρ is water density, q is the water flux and f_w is the sink/source term. For the mechanical problem, ignoring the inertial terms, the momentum balance equation simplifies into the equilibrium of stresses

$$\nabla.\sigma + f = 0, \qquad (7.2)$$

where σ is the stress tensor and f is the vector of body forces. Darcy's law is used to compute the flow of water in the system and writes

$$q = -\frac{k}{\mu}(\nabla p + \rho g \nabla z), \qquad (7.3)$$

where k is permeability, μ is water viscosity and g is gravity.

The rock matrix and the fracture are considered as two different materials having distinct properties listed in Table 7.1. Fracture permeability varies as a function of aperture, b, following the cubic law (Olivella and Alonso, 2008)

$$k = k_{matrix} + \frac{b^3}{12a}, \qquad (7.4)$$

$$b = b_0 + \Delta b, \qquad (7.5)$$

$$\Delta b = a\Delta\epsilon = a(\epsilon - \epsilon_o),$$
$$for\ \epsilon > \epsilon_o, \qquad (7.6)$$

where k_{matrix} is the intrinsic permeability of the porous material filling the fracture, a is the spacing of the fractures, and ϵ and ϵ_o are the volumetric strain and reference volumetric strain, respectively. The initial aperture (b_0) is 10 μm and the spacing between the fractures (a) is 10 cm, i.e., only one fracture is present in the continuum medium representing the fracture.

The constitutive behaviour of fractures is governed by a plastic model that includes dilatancy and strain softening. The yield function is

$$F = \sigma_m . sin\phi(\eta) + \left(cos\theta - \frac{1}{\sqrt{3}}sin\theta . sin\phi(\eta)\right).\sqrt{J_2} - c(\eta).cos\phi(\eta) \qquad (7.7)$$

and the plastic potential

$$G = \alpha.\sigma_m.sin\psi + \left(cos\theta - \frac{1}{\sqrt{3}}sin\theta.sin\psi\right).\sqrt{J_2} - c(\eta).cos\psi, \qquad (7.8)$$

while the loading-unloading conditions are

$$\Phi(F) = F^m \ for \ F \geq 0 \text{ and } \Phi(F) = 0 \ for \ F < 0. \qquad (7.9)$$

The previous equations express the plastic behaviour as a combination of invariants of the stress tensor, i.e.,

$$\sigma_m = (\sigma_{xx} + \sigma_{yy} + \sigma_{zz})/3;$$
$$J_2 = \frac{1}{6}\sqrt{(\sigma_{xx} - \sigma_{yy})^2 + (\sigma_{yy} - \sigma_{zz})^2 + (\sigma_{zz} - \sigma_{xx})^2 + 6(\tau_{xy}^2 + \tau_{yz}^2 + \tau_{zx}^2)};$$
$$\theta = \frac{1}{3}sin^{-1}\left(-\frac{3\sqrt{3}J_3}{2\sqrt{J_2}^3}\right);$$
$$J_3 = S_x S_y S_z + 2\tau_{xy}\tau_{yz}\tau_{zx} - S_x\tau_{yz}^2 - S_y\tau_{xz}^2 - S_z\tau_{xy}^2.$$

In the plastic model, ψ is the dilatancy angle, c the cohesion, and the friction angle ϕ

$$\phi(\eta) = \left\{\phi^{peak}, \square \leq 0 \ ; \square^{peak} + \left(\frac{\phi^{res} - \phi^{peak}}{\eta^*}\right).\eta, 0 \leq \eta \leq \eta^* \ ; \square^{res}, \square^* \leq \eta\right\}, \qquad (7.10)$$

where

$$\eta = \sqrt{\frac{3}{2}.[(\epsilon_{xx}^p - \epsilon_m^p)^2 + (\epsilon_{yy}^p - \epsilon_m^p)^2 + (\epsilon_{zz}^p - \epsilon_m^p)^2 + (\frac{1}{2}.\gamma_{xy}^p)^2 + (\frac{1}{2}.\gamma_{yz}^p)^2 + (\frac{1}{2}.\gamma_{zx}^p)^2]} \qquad (7.11)$$

and $\epsilon_m^p = \frac{1}{3}.(\epsilon_{xx}^p + \epsilon_{yy}^p + \epsilon_{zz}^p);$

$\square$ is a parameter for plastic potential, ϵ^p is the plastic strain tensor and γ is the shear component of the plastic strain tensor.

The rock matrix in the reservoir geometry (Figure 7.1A) is ideally divided into two sectors separated by the fracture – one to the left-hand side of the fracture, and another to the right-hand side of the fracture. Positive x is towards the right and positive y is upwards in Fig. 7.1A. To allow for large shear slip of the fracture upon reactivation, the boundaries of the right-hand side of the fracture are fixed, while constant stress is applied to the boundaries of the left-hand side. The minimum horizontal stress (σ_x) is 63 MPa, the maximum horizontal stress (σ_y) is 104 MPa and the vertical stress (σ_z) is 100 MPa. A constant pore pressure of 40 MPa is applied over the entire domain.

The finite element code CODE_BRIGHT (Olivella et al., 1994; 1996) is used to numerically simulate the fully coupled HM models. The mesh is composed of a total of 3625 quadratic elements, being fine near the injection well and getting gradually coarser away from it along the fracture. The size of the elements is 3.33 x 10^{-2} m x 5.52 x 10^{-2} m near the well, 3.33 x 10^{-2} m x 6.68 m at the edges of the fracture, and 56.1 m x 50.0 m along the boundaries of the model.

7.3 Results

The injection protocol affects the HM response of the fracture to hydraulic stimulation. Despite the same volume of water is injected in all cases, pore pressure build-up and the induced poromechanical stresses differ in each case. The difference is highlighted for the injection rate of 0.1 kg/s/m, which leads to purely elastic deformation in the cyclic-injection scheme, a slight fracture reactivation close to the injection well in the step-rate scheme, and a full fracture reactivation in the constant-rate scheme (compare Figures 7.1B, 7.1C and 7.1D). As the injection rate is increased, the maximum pore pressure increases as well, leading to fracture reactivation in all cases (Figures 7.1E-7.1J). The pressure build-up does not scale linearly with the injection rate because fracture permeability is enhanced with the cube of fracture aperture (Eq. 7.4). The fracture aperture increases during injection following two distinct mechanisms: pressure build-up and slip-induced dilatancy (Yeo et al., 1998). The larger the dilatancy angle, the larger the permeability enhancement and thus, the lower the resulting pressure build-up. As a result, the length of the fracture that becomes reactivated decreases as the dilatancy angle increases (Figures 7.1B, 7.1E-J). For the largest dilatancy angle, i.e., 10°, a high-permeability region is created close to the injection well, but the permeability enhancement occurs in a relatively small area. In contrast, very low dilatancy angles, i.e., 0.1°, lead to a larger area undergoing permeability enhancement, but with the resulting permeability being two orders of magnitude lower than for the largest dilatancy angle. The magnitude of the permeability enhancement is similar for the three injection schemes, but the extent of the stimulated region depends on the scheme. The cyclic-injection scheme, closely followed by the constant-rate scheme, produces the largest fracture length in which permeability is enhanced at the end of the stimulation. The step-rate scheme yields the smallest stimulated fracture length, especially for low dilatancy angles. The pressure changes that occur within the fracture as a result of slip-induced dilatancy are accompanied by pore pressure changes in the surrounding rock matrix.

Shear slip induces additional pore pressure changes resulting from an undrained response of the rock matrix to the deformation caused by fracture reactivation (Vilarrasa et al., 2021). The difference in the pore pressure distribution between a stimulation that only induces elastic strain and another one that reactivates the fracture is displayed in Figure 7.2. The pore pressure distribution is purely diffusive when the fracture behaves elastically (Figure 7.2A). The poromechanical response to fracture pressurization is observed at the tips of the pressure diffusion front, where a pressure drop occurs because of deformation-induced pressure changes analogous to the Noordbergum effect (Hsieh, 1996). Once the fracture reaches failure conditions, it undergoes irreversible shear slip, which contracts the rock in front of the slip direction and expands the rock behind the slipped area. As a result, pore pressure increases where the rock is contracted and decreases where it is expanded (Figure 7.2B). Such pore pressure changes, which have a similar magnitude to the ones induced by injection within the fracture, are transient and dissipate after several days for the rock properties considered here. The dissipation time is inversely proportional to the rock permeability and, thus, it could give rise to delays of weeks or months in a very low-permeability matrix.

Shear slip also induces changes in the shear stress at and around the fracture (Figure 7.3). The slipped area undergoes a shear stress drop that inhibits further reactivation. In contrast, the trailing edges of the slipped area experience an increase in shear stress that brings the stress state closer to failure conditions. However, stability is maintained at the edges shortly after slip because the deformation-induced pore pressure changes yield a pressure drop in these regions (compare Figures 7.2B and 7.3). Subsequently, as deformation-induced pore pressure changes dissipate, failure conditions may be reached because the shear stress changes remain (Vilarrasa et al., 2021). Such post-injection reactivation is observed in the cyclic-injection protocols, in which the stimulated region of the fracture extends at the tips during the no-injection intervals. This reactivation happens due to pore pressure diffusion towards the unstimulated regions of the fracture where shear stress has increased. At the

end of the cyclic-stimulation protocol of rate 0.3 kg/s/m, the tips of the reactivated regions of the fracture are still weak (Figure 7.3), and the shear stress is sufficient to induce slip in the post-injection interval (Kamali and Ghassemi, 2016).

The amount of slip induced in the fracture during stimulation operations varies with the type of injection protocol and the injection rate used. The cyclic-injection protocol with a rate of 0.1 kg/s/m induces negligible slip (purely elastic) until the end of injection (Figure 7.4C). In the rest of the injection rates, the step-rate injection protocols induce less slip than the constant and cyclic protocols (Figures 7.4D-7.4I). In the step-rate injection, injection starts at a rate which is 20% of the rate injected in the constant and cyclic-stimulation protocols and gradually increases until it reaches the maximum rate, that is equal to the rate of injection in the constant and cyclic protocols. As a result, the pore pressure front progresses slower in the models with step-rate injection, accumulating less slip before the final injection rate is reached. During the final step, the amount of slip induced is considerable (Figures 7.5E and 7.5H), but the final cumulated slip at the end is lower than in the other protocols (Figures 7.4E, 7.4H). The cyclic-injection protocols induce slip on a larger portion of the fracture than the other protocols due to the slip induced by the pore pressure diffusion at the edges of the reactivated region of the fracture in its alternate no-injection intervals (Figures 7.4F, 7.4I). The amount of injected water required to cause a significant slip in the fracture is larger than in the constant-rate protocol for an injection rate of 0.2 kg/s/m (compare Figures 7.5D and 7.5F), but they become similar as the injection rate increases to 0.3 kg/s/m (compare Figures 7.5G and 7.5I). This delay is caused by the pore pressure reduction that occurs during the no-injection intervals, retarding the time at which the critical pressure for reactivation is reached. Once the fracture is reactivated for the first time, a significant shear slip occurs at the beginning of each cycle. The constant-rate injection protocols lead to the earliest fracture reactivation (Figures 7.5A, 7.5D and 7.5G). Despite the differences in the time of reactivation and differences in the slip magnitude, the maximum slip rate, which coincides with the onset of shear slip, is very similar for the three protocols at injection rates higher than 0.1 kg/s/m (Figure 7.5).

7.4 Discussion

We have conducted a numerical study to understand the mechanisms that differentiate the various stimulation protocols. Our results show that both permeability enhancement and injection-induced slip are influenced by the stimulation protocol. We observe a marked difference in the response between the injection rates of 0.1 kg/s/m and 0.2 kg/s/m for all the tested protocols (Figures 7.1B-7.1G and Figures 7.4A-7.4F). Simulation results suggest the existence of a lower limit of injection rate for which the fracture stimulation will not guarantee enough permeability. When the injection rate is lower than a given threshold (which intrinsically depends on the hydromechanical properties of the rock and fracture, fracture orientation with respect to the principal stresses and in-situ initial stress state), the injection-induced pressure build-up might not be sufficient to reactivate a fracture, which instead behaves in a purely elastic manner (Figure 7.1D and Figure 7.4C). Above that threshold, the fracture reactivates at a given point, accumulating shear slip and enhancing permeability as a result of dilatancy.

Dilatancy enhances permeability of the sheared region between one to four orders of magnitude (Figure 7.1). Low dilatancy angles give rise to a relatively low permeability enhancement, but the length of the fracture with enhanced permeability is larger than for high dilatancy angles. As a result, the injection pressure for a given flow rate may become larger, but also the chances of establishing a hydraulic connection between the two wells of a doublet. Taking into account that dilatancy decreases with normal stress, the dilatancy angle becomes low at the typical depths of EGS (Xie and Min, 2021). For a given value of the dilatancy angle and injection rate (0.2 kg/s/m or 0.3 kg/s/m), the maximum achieved permeability is independent of the injection protocols. Instead, the protocol affects the extent

of the fracture that becomes stimulated, being the maximum for the cyclic injection (Figures 7.1E-7.4J). Yet, fracture reactivation may continue after shut-in in the constant and step-rate injection protocols, which may eventually lead to similar stimulated fracture lengths. The post-injection reactivation is caused by a combination of increased slip-induced shear stress and a reduction of the pore pressure, which drops during injection as a result of deformation-induced pore pressure changes (Vilarrasa et al., 2021).

Simulation results show that the cyclic-injection protocols also induce the largest amount of slip on the fracture (Figures 7.4F and 7.4I). The largest slip observed in the cyclic injection protocols seem to suggest a higher potential of inducing larger earthquakes than the other schemes. However, our quasi-static analysis cannot differentiate between a-seismic and co-seismic dynamic slip and the final size of runaway rupture requires full dynamic simulations. The slip rate is very similar for all protocols for a given injection rate, which hints at a similar timing of fault rupture. In our simulations, the maximum slip velocity is four orders of magnitude lower than the one for the onset of dynamic rupture, i.e., 0.1 m/s (Rubin and Ampuero, 2005), which could indicate that the system has not reached favourable conditions for runaway ruptures. Our results have shown that the influence of the adopted stimulation protocol is marginal. We have found no evidence that the cyclic injection protocol is an effective strategy to control induced seismicity (Zang et al., 2019; Niemz et al., 2020). This result seems to be supported by the failure of the cyclic stimulation protocol to prevent the large event that occurred in Pohang (Ellsworth et al., 2019).

7.5 Conclusions

We have studied the efficiency of three protocols of hydraulic stimulation in a single pre-existing fracture. The injection rate should be sufficiently high, so that the fracture is reactivated and irreversible shear slip occurs, enhancing fracture permeability due to dilation. Permeability enhancement increases with the dilatancy angle, but is concomitant with a decreasing stimulated fracture length. The cyclic-injection protocol enhances the permeability of a larger area of the fracture than the other protocols and the step-rate injection protocol induces the least amount of slip in the fracture. Nonetheless, the differences remain within the same order of magnitude and, thus, no significant differences between the hydraulic stimulation protocols exist. It is likely that de-risking induced seismicity will not be achieved with the current stimulation protocols that have been tested.

References:

Andrés, S., Santillán, D., Mosquera, J.C., Cueto-Felgueroso, L., Thermo-Poroelastic Analysis of Induced Seismicity at the Basel Enhanced Geothermal System. *Sustainability, 11*, 6904 (2019).

Abe, A. and Horne, R. N., Investigating fracture network creation and stimulation mechanism of EGS reservoirs. *Geothermics, 107* (2023).

Brace, W.F., Paulding E.T., Scholtz C., Dilatancy in the fracture of crystalline rocks. *J Geophys Res*, 71 pp. 3939-3953 (1966).

Brown, D., Duchane, D., Heiken, G., Hriscu, V., Mining the Earth's Heat: Hot Dry Rock Geothermal Energy, *Springer* (2012).

Cueto-Felgueroso, L., Santillán, D., Mosquera, J. C. Stick-slip dynamics of flow-induced seismicity on rate and state faults. *Geophysical Research Letters*, *44*(9), 4098-4106 (2017).

De Simone, S., Carrera, J., Vilarrasa, V., Superposition approach to understand triggering mechanisms of post-injection induced seismicity. *Geothermics*, *70*, 85-97 (2017).

Deichmann, N., Kraft, T., Evans, K. F., Identification of faults activated during the stimulation of the Basel geothermal project from cluster analysis and focal mechanisms of the larger magnitude events. *Geothermics*, *52*, 84-97 (2014).

Ellsworth, W. L., Giardini, D., Townend, J., Ge, S., Shimamoto, T., Triggering of the Pohang, Korea, Earthquake (Mw 5.5) by Enhanced Geothermal System Stimulation, *Seismological Research Letters,* 90 (5): 1844–1858 (2019).

Ghassemi, A. A review of some rock mechanics issues in geothermal reservoir development. *Geotechnical and Geological Engineering*, *30*(3), 647-664 (2012).

Giardini, D., Geothermal quake risks must be faced. *Nature*, *462*(7275), 848-849 (2009).

Häring, M. O., Schanz, U., Ladner, F., Dyer, B. C., Characterisation of the Basel 1 enhanced geothermal system, *Geothermics*, 37 (5): 469-495 (2008).

Hsieh, P. A., Deformation-induced changes in hydraulic head during ground-water withdrawal. *Groundwater*, *34*(6), 1082-1089 (1996).

Kamali, A., Ghassemi, A., Analysis of Natural Fracture Shear Slip and Propagation in Response to Injection, Proceedings of 41st Workshop on Geothermal Reservoir Engineering, Stanford (2016).

Kim, K., Makhnenko, R. Y., Coupling between poromechanical behavior and fluid flow in tight rock. *Transport in Porous Media*, *135*(2), 487-512 (2020).

Kim, K. H., Ree, J. H., Kim, Y., Kim, S., Kang, S. Y., Seo, W., Assessing whether the 2017 M w 5.4 Pohang earthquake in South Korea was an induced event. *Science*, *360*(6392), 1007-1009 (2018).

Lepillier, B., Yoshioka, K., Parisio, F., Bakker, R., Bruhn, D. Variational Phase-field modeling of hydraulic fracture interaction with natural fractures and application to Enhanced Geothermal Systems. Journal of Geophysical Research: Solid Earth, 125(7), p.e2020JB019856 (2020).

Majer, E. L., Baria, R., Stark, M., Oates, S., Bommer, J., Smith, B., Asanuma, H., Induced Seismicity associated with Enhanced Geothermal Systems, *Geothermics,* 36 (3): 185-222 (2007).

McClure, M.W., Horne, R.N., An investigation of stimulation mechanisms in Enhanced Geothermal Systems. *Int J Rock Mech Min Sci,* 72:242–60 (2014).

McGarr, A., Maximum magnitude earthquakes induced by fluid injection. *J. Geophys. Res.* 119:1008–1019 (2014).

Mukuhira, Y., Asanuma, H., Niitsuma, H., Häring, M. O., Characteristics of large-magnitude microseismic events recorded during and after stimulation of a geothermal reservoir at Basel, Switzerland. *Geothermics*, *45*, 1-17 (2013).

Mukuhira, Y., Dinske, C., Asanuma, H., Ito, T., Häring, M. O., Pore pressure behavior at the shut-in phase and causality of large induced seismicity at Basel, Switzerland. *Journal of Geophysical Research: Solid Earth*, *122*(1), 411-435 (2017).

Niemz, P., Cesca, S., Heimann, S., Grigoli, F., von Specht, S., Hammer, C., Zang, A., Dahm, T. Full-waveform-based characterization of acoustic emission activity in a mine-scale experiment: a comparison of conventional and advanced hydraulic fracturing schemes. *Geophysical Journal International*, 222(1), pp.189-206 (2020).

Olivella, S., Alonso, E. E., Gas flow through clay barriers. *Géotechnique*, *58*(3), 157-176 (2008).

Olivella, S., Carrera, J., Gens, A., Alonso, E. E., Non-isothermal multiphase flow of brine and gas through saline media. *Transp. Porous Media* 15: 271–293 (1994).

Olivella, S., Gens, A., Carrera, J., Alonso, E. E., Numerical formulation for a simulator (CODE_BRIGHT) for the coupled analysis of saline media. *Eng. Comput.* 13: 87–112 (1996).

Pampillon, P., Santillán, D., Mosquera, J. C., Cueto-Felgueroso, L. Dynamic and quasi-dynamic modeling of injection-induced earthquakes in poroelastic media. *Journal of Geophysical Research: Solid Earth*, *123*(7), 5730-5759 (2018).

Parisio, F. Yoshioka, K. Modeling fluid reinjection into an enhanced geothermal system. *Geophysical Research Letters*, 47(19), p.e2020GL089886 (2020).

Rubin, A. M., Ampuero, J. P. Earthquake nucleation on (aging) rate and state faults. *Journal of Geophysical Research: Solid Earth*, *110*(B11) (2005).

Segall, P., Lu, S. Injection-induced seismicity: Poroelastic and earthquake nucleation effects. *Journal of Geophysical Research: Solid Earth*, *120*(7), 5082-5103 (2015).

Verdon, J. P., Bommer, J. J. Green, yellow, red, or out of the blue? An assessment of Traffic Light Schemes to mitigate the impact of hydraulic fracturing-induced seismicity. *Journal of Seismology*, *25*(1), 301-326 (2021).

Vilarrasa, V., Koyama, T., Neretnieks, I., Jing, L. Shear-induced flow channels in a single rock fracture and their effect on solute transport. *Transport in Porous Media*, *87*(2), 503-523 (2011).

Vilarrasa, V., De Simone, S., Carrera, J., Villaseñor, A. Unraveling the causes of the seismicity induced by underground gas storage at Castor, Spain. *Geophysical Research Letters*, *48*(7), e2020GL092038 (2021).

Xie, L., Ki-Bok, M., Yoonho, S. Observations of hydraulic stimulations in seven enhanced geothermal system projects. *Renewable Energy* 79: 56-65 (2015).

Xie, L., Min, K. B. Discrete element modelling of multi-stage hydroshearing stimulation in Enhanced Geothermal System. *Geothermics*, *95*, 102135 (2021).

Yeo, I. W., De Freitas, M. H., Zimmerman, R. W. Effect of shear displacement on the aperture and permeability of a rock fracture. *International Journal of Rock Mechanics and Mining Sciences*, *35*(8), 1051-1070 (1998).

Yeo, I. W., Brown, M. R. M., Ge, S., Lee, K. K. Causal mechanism of injection-induced earthquakes through the Mw 5.5 Pohang earthquake case study. *Nature Communications*, *11*(1), 2614 (2020).

Zang, A., Zimmermann, G., Hofmann, H., Stephansson, O., Min, K. B., Kim, K. Y. How to reduce fluid-injection-induced seismicity. *Rock Mechanics and Rock Engineering*, *52*(2), 475-493 (2019).

Zareidarmiyan, A., Parisio, F., Makhnenko, R. Y., Salarirad, H., Vilarrasa, V. How equivalent are equivalent porous media? *Geophysical Research Letters*, *48*(9), e2020GL089163 (2021).
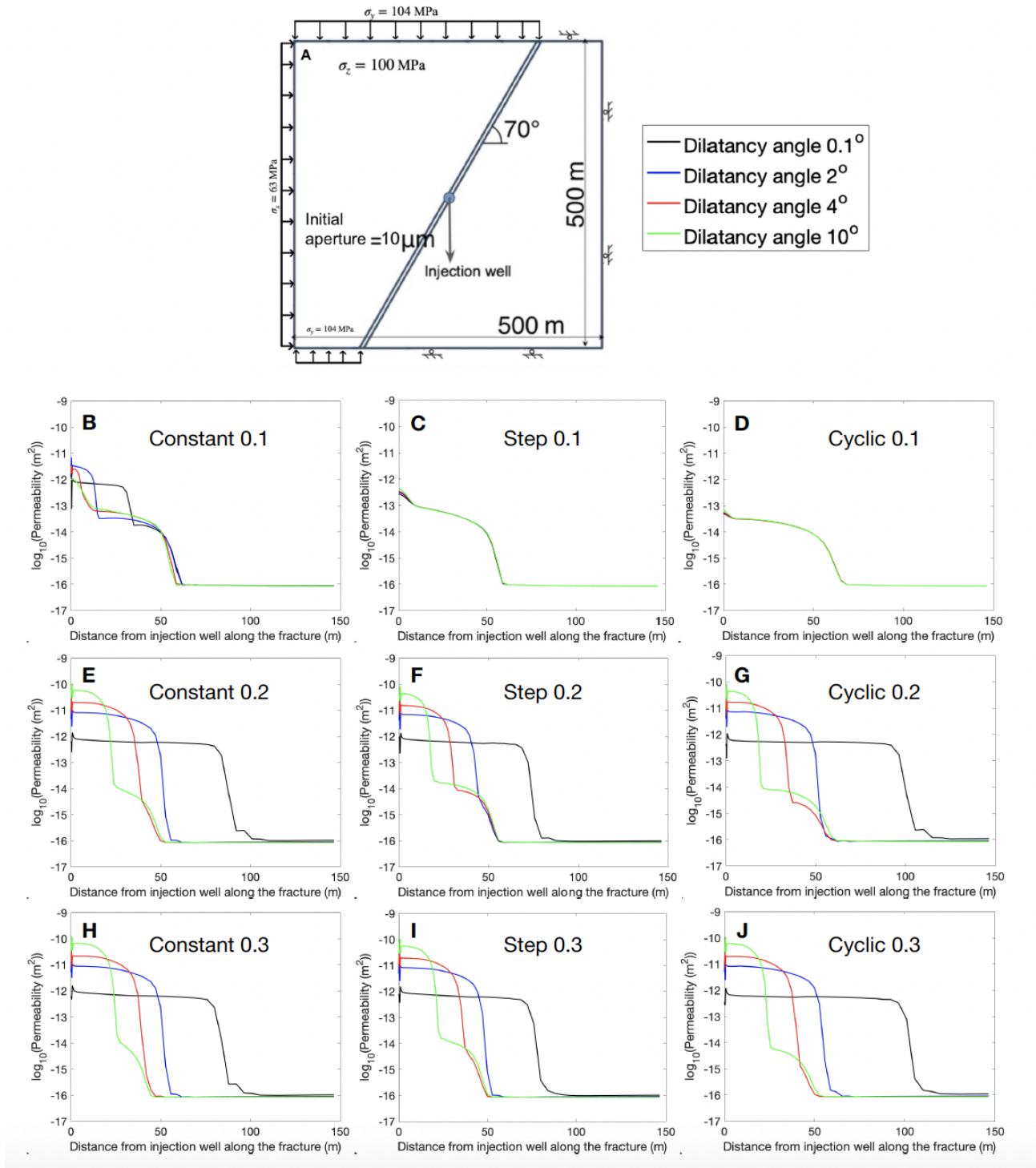
Figures

Figure 7.1: (A) Geometry of the model and legend for plots **(B-J)**, which represent the permeability as a function of the dilatancy angle along the fracture at the end of the stimulation for various injection schemes (constant (B, E and H), step (C, F and I) and cyclic (D, G and J)) and flow rates (0.1 (B-D), 0.2 (E-G) and 0.3 (H-J) kg/s/m) as mentioned in the plots.
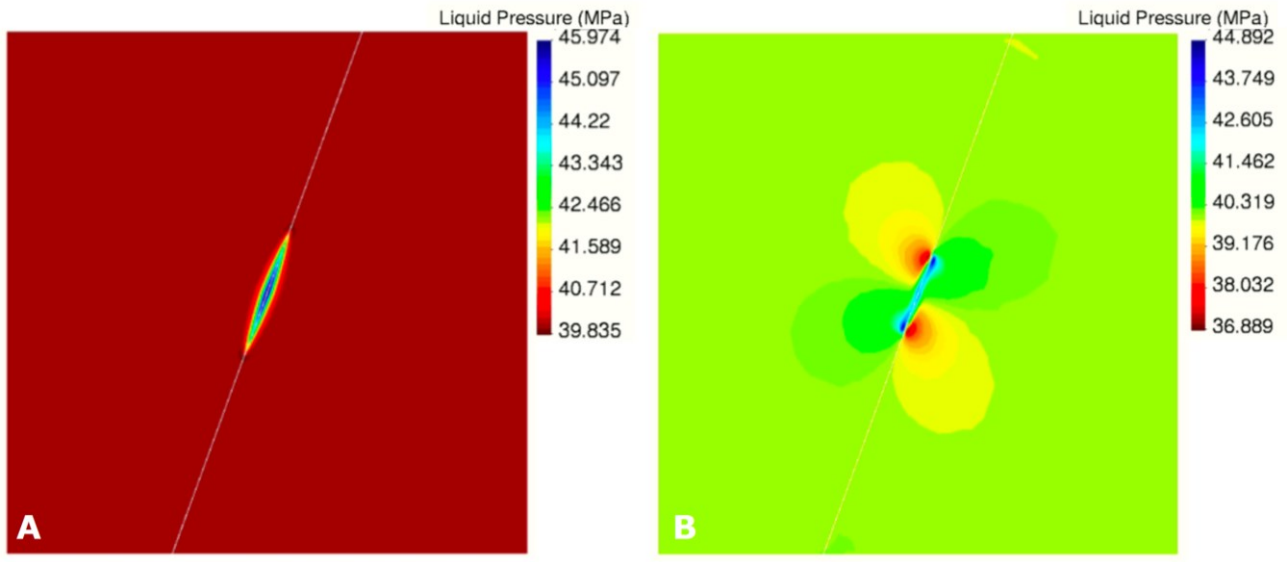
Figure 7.2: Pore pressure distribution at the end of stimulation for the cyclic injection scheme with injection rates of (A) 0.1 kg/s/m and (B) 0.3 kg/s/m. Pore pressure distribution is indicative of elastic deformation in (A) and irreversible fracture reactivation in (B).
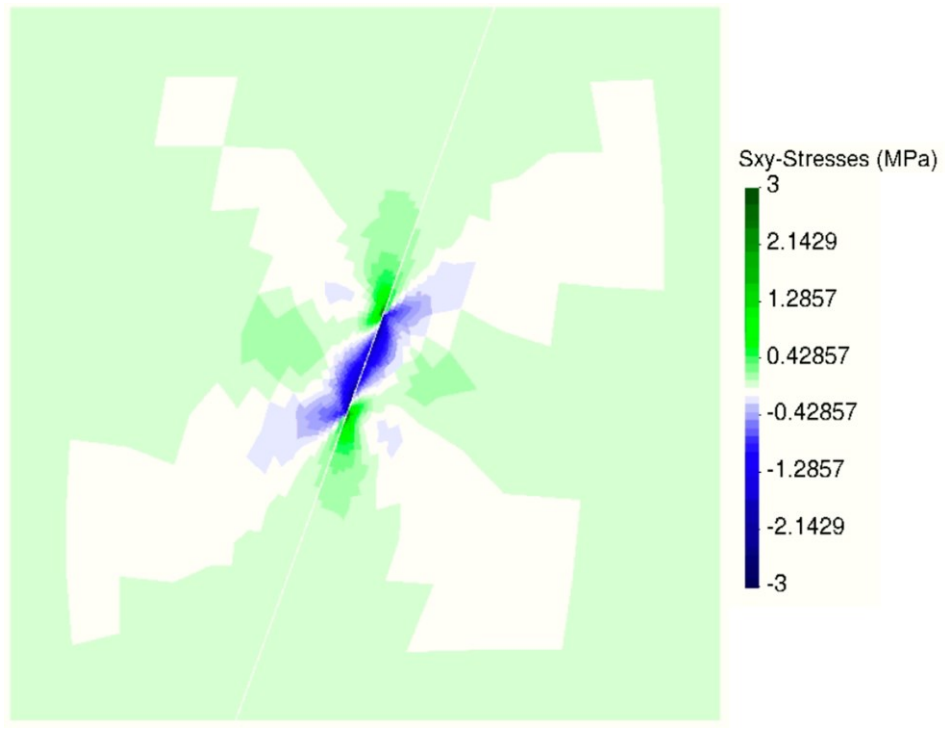

Figure 7.3: Shear stress distribution over the reservoir at the end of the cyclic injection scheme with the injection rate of 0.3 kg/s/m.
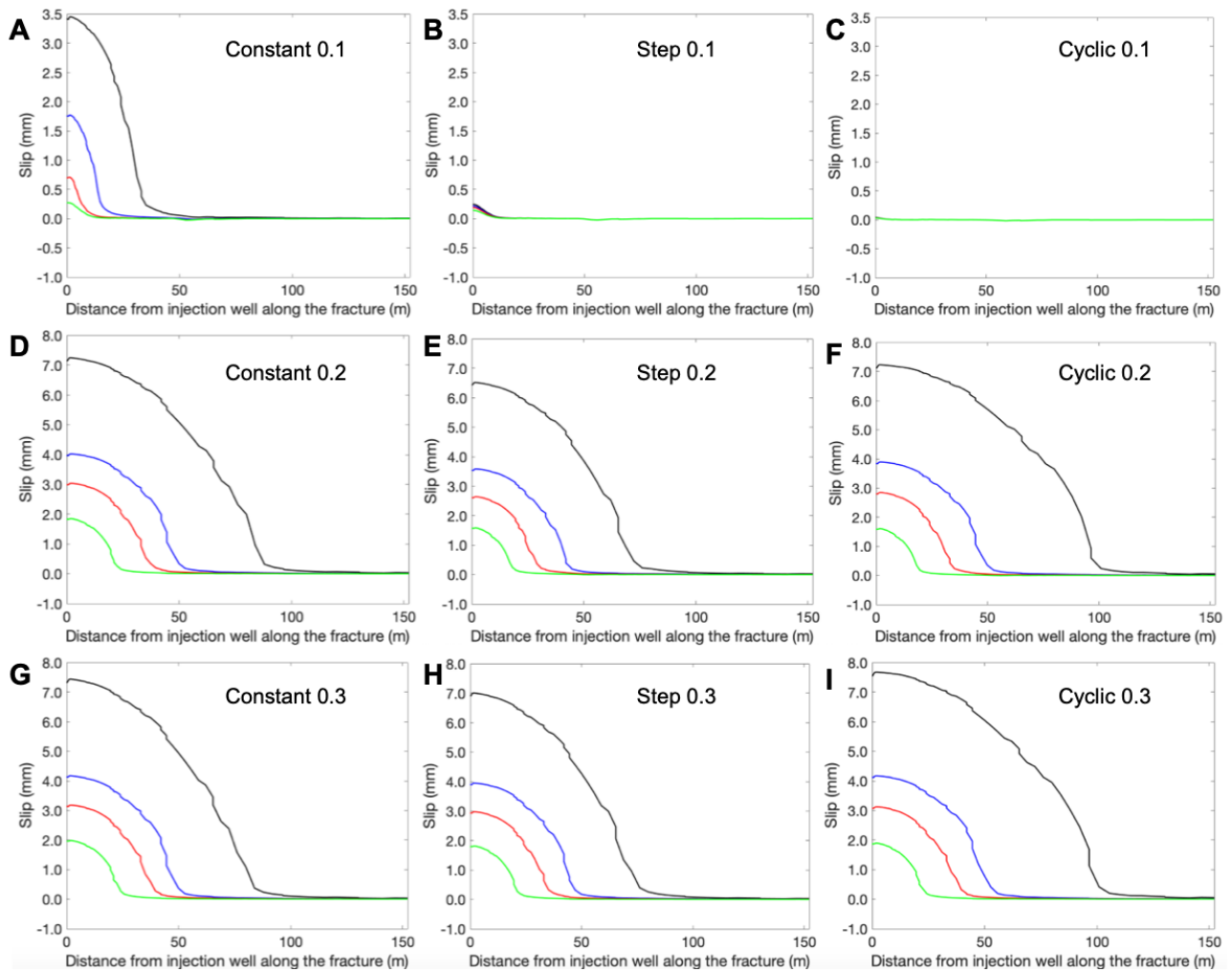
Figure 7.4: A, B, C, D, E, F, G, H and I display the slip along the fracture as a function of dilatancy for constant rate (A, D and G), step rate (B, E and H) and cyclic injection (C, F and I) at a rate of 0.1 (A, B and C), 0.2 (D, E and F) and 0.3 kg/s/m (G, H and I) at the end of the stimulations (the legend is the same as in Figure 7.1A).
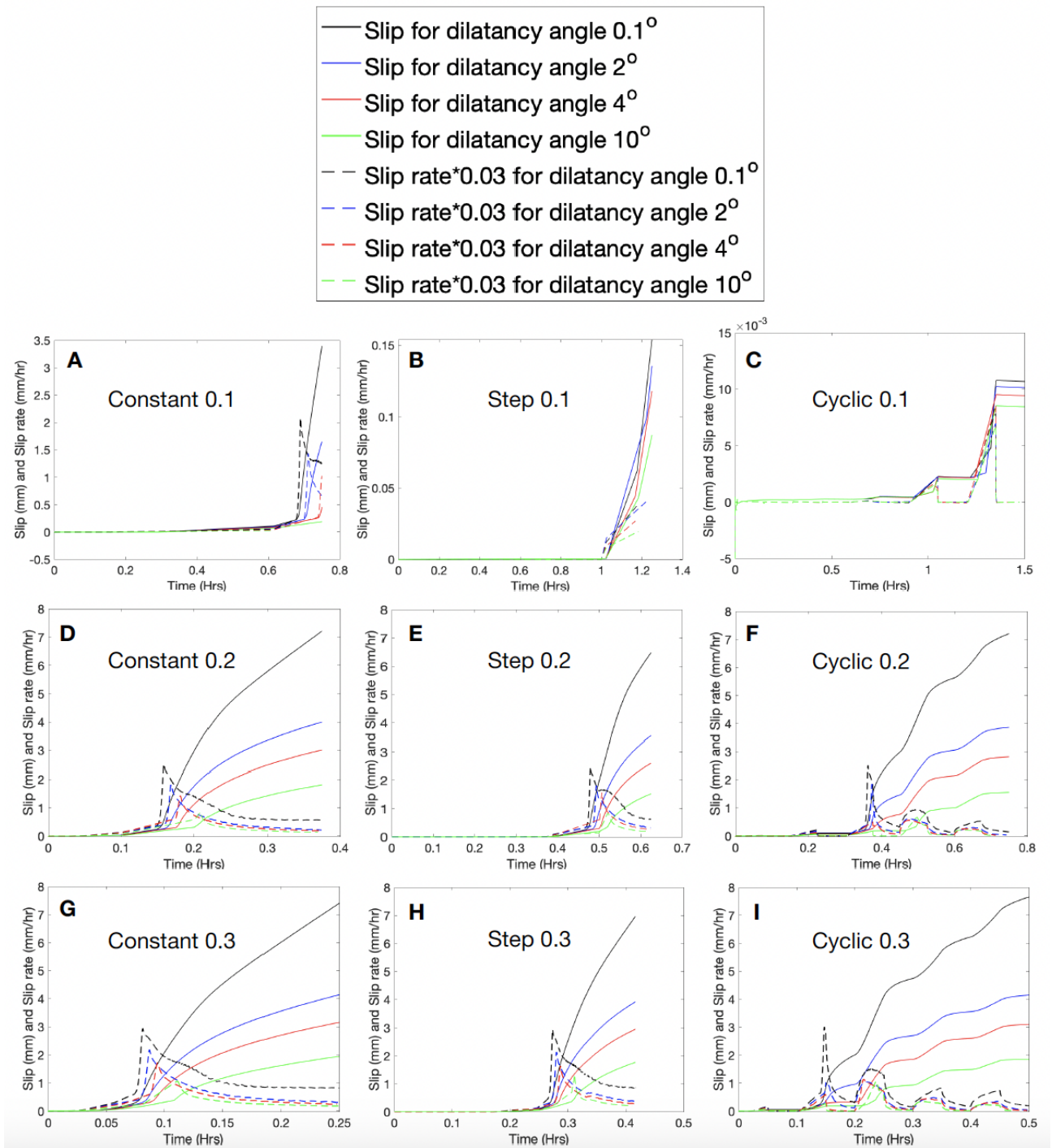
Figure 7.5: A, B, C, D, E, F, G, H and I display the slip and slip rate evolution as a function of dilatancy for constant rate (A, D and G), step rate (B, E and H) and cyclic injection (C, F and I) at a rate of 0.1 (A, B and C), 0.2 (D, E and F) and 0.3 kg/s/m (G, H and I).

Tables

Table 7.1. Material properties of rock matrix the fracture

Material Properties	Rock Matrix	Fracture
Permeability (m^2)	$2.5 \cdot 10^{-18}$	$8.33 \cdot 10^{-17}$
Porosity (−)	0.005	0.0001
Young's modulus (GPa)	60	2.8
Poisson's ratio (−)	0.3	0.44
Biot's Coefficient (−)	0.5	1
1/Viscosity (s⁻¹ MPa⁻¹)	-	$1 \cdot 10^{-4}$
Maximum cohesion (MPa)	-	0.1
Residual cohesion (MPa)	-	0.1
Maximum friction angle (°)	-	36
Residual friction angle (°)	-	24
Dilatancy angle (°)	-	$0.1,2,4\ and\ 10$
Critical value of softening parameter (−)	-	0.0185